Scholar Publishing Group
International Journal of Engineering Technology and Construction
https://doi.org/10.38007/IJETC.2022.030105
ISSN 2789-7176 Vol. 3, Issue 1: 62-79

Anti-Salt Frost Erosion Performance of Photocatalytic Nano-Material Bi2WO6 in Architectural Coatings

Chadie Altrjmane*

Near East University, Turkey

**corresponding author*

Keywords: Photocatalytic Nano-Material Bi2WO6, Architectural Coatings, Salt-Freeze Erosion Resistance, Freeze-Thaw, Dynamic Elastic Modulus

Abstract: With the rapid development of the construction industry and real estate industry, related important chemical building materials products, architectural coatings, have also grown rapidly and become an important part of the coating industry. This research mainly discusses the salt-freeze-stripping resistance test of the photocatalytic nano-material bismuth tungstate in architectural coatings. Using sodium tungstate and bismuth nitrate as the tungsten source and bismuth source respectively, the two solutions are mixed to form a precursor solution, and the precursor is placed in a stainless steel reactor. After a certain hydrothermal time and temperature, bismuth tungstate nanoflowers are prepared. XRD, SEM, FT-IR, DRS and other characterization methods were used to analyze the morphology and structure of the product, and the positions of the band gap, conduction band and valence band of bismuth tungstate were determined by calculation. Photocatalytic degradation effect fuels such as MO and MB. The degree of internal damage during the ultrasonic transmission time is reflected by the relative change of the dynamic elastic modulus before and after freezing and thawing. The relative change value of the dynamic elastic modulus is determined by measuring the transmission time of the ultrasonic wave passing through the parallel axis 25mm from the surface of the test piece. UV-2450 spectrophotometer, the standard reagent is high-purity BaSO4. Characterize the light absorption characteristics according to the light absorption of the sample in the wavelength range of 200-800nm. Before the sample is pre-saturated,before freezing and thawing, the ultrasonic transmission time was measured after 14, 28, 42 and 56 freeze-thaw cycles. The measuring instrument used NM-4A-I non-metal ultrasonic detection analyzer. The penetration quality and penetration depth of the architectural coating deicing salt solution with a bismuth tungstate content of 30% is greater than that of the architectural coatings with a bismuth tungstate content of 16.7%. This research will promote the application of nanomaterials in architectural coatings.

1. Introduction

Bismuth tungstate, as a new semiconductor material, shows good response under visible light

and its high photogenerating carrier recombination ratio greatly improves the photocatalytic performance. Therefore, the combination of bismuth tungstate responsive to visible light and TiO_2 nanowires with high electron movement speed will block the recombination of electrons and holes generated by light, and solve the bottleneck problem in the application of photocatalyst.

Nanomaterials are widely used in new construction materials, new coatings, deterioration of construction wastes, environmental treatment and other fields due to their unique photoelectric characteristics, excellent oxidation resistance and excellent photostability. This makes it possible to conduct more detailed research on its catalytic mechanism, better combine with the field of industrial construction, and lay a theoretical foundation for the application of photocatalytic nanomaterials in the field of industrial construction.

Nanomaterials have attracted great attention from researchers because of their special physical and chemical properties. Kumar S G believes that metal oxide semiconductors (TiO_2, WO_3 and ZnO) find unparalleled opportunities for wastewater purification in UV/visible light, due in large part to their different properties, such as stability, non-toxicity, ease of preparation, suitable band edge location and easy generation of reactive oxygen species in aqueous media. However, the long-term failure of these photocatalysts stems from stumbling blocks such as fast charge carrier recombination and weak visible light response. In his research, by calibrating and literally customizing the surface's electronic structure, examples include impurity doping, deposition of precious metals, electronic integration with other compounds (dyes, polymers, inorganic complexes, and simple chelating ligands), modification with carbon nanostructures, design of exposed small planes, and tailoring using layered forms to overcome their key shortcomings [1]. Ma J reported a composite photocatalyst $Bi_2O_2CO_3$/ Bismuth tungstate successfully prepared by a two-step hydrothermal process assisted by Ag nanoparticles. The use of Ag nanoparticles promotes the production of $Bi_2O_2CO_3$ by oxidizing ethylene glycol and obtaining the most suitable heterostructure. The synthesized $Bi_2O_2CO_3$/ Bismuth tungstate photocatalyst has larger specific surface area than pure Bi_2O_3 and pure bismuth tungstate samples. The complex structure of $Bi_2O_2CO_3$/ Bismuth tungstate is favorable for the separation of photogenerated electrons and holes because the photoluminescence intensity of the emission peak is significantly reduced. The $Bi_2O_2CO_3$/ Bismuth tungstate -3% composite has a large specific surface area and a low photoelectron-hole pair recombination ratio, which shows the highest photocatalytic activity in the photodegradation of gaseous pollutants under visible light ($\lambda > 420$ nm). The photocatalytic activity of $Bi_2O_2CO_3$/ Bismuth tungstate -3% composite is 2.05, 3.41 and 10.19 times that of $Bi_2O_2CO_3$/ Bismuth tungstate, pure Bi_2O_3 and pure Bismuth tungstate, respectively [2]. Bansal A described the first successful use of ectopic copper (0) nanoparticles as an effective catalyst, using toluene as an effective solvent when water-doped SET-LRP. Single-electron transfer mediated LRP (SET-LRP) of methyl methacrylate (MMA) was performed using Cu(0) nanoparticles (Cu(0) nanoparticles at about 5 nm as catalysts with different nitrogen (N) ligands. A two-phase water-toluene system was used as the reaction medium. By changing the catalyst concentration (0.15 PPM to 28.5 PPM) and change the monomer, initiator and the molar ratios of N - ligand research of polymerization five methyl diethylene triamine (PMDETA), N, N, N ', N '- methyl - 1, 6 - hexamethylenediamine (TMHDA),N,N,N',N' -tetramethylenediamine (TMEDA) and N, N-dimethylhexadecane amine (DMHA)). Among the various N ligands studied, PMDETA provided the best control of molecular weight, while TMHDA provided the worst control, resulting in polydispersity of 1.15 and 2.11 at high monomer conversion rates, respectively [3].Ratova M prepared titanium dioxide bismuth tungstate composite by pulsed DC reactive magnetron sputtering of bismuth and tungsten metal targets onto anatase and rutile titanium dioxide nanoparticles in an argon/oxygen atmosphere. He

was able to deposit bismuth tungstate onto a loose powder rather than a solid substrate using oscillating bowls placed beneath two magnetrons arranged in a coplanar closed field configuration. The atomic ratio of the bismuth/tungsten coating is controlled by varying the power applied to each target. The effects of bismuth tungstate coating on the phase, optical and photocatalytic properties of TO_2 were studied by X-ray diffraction, energy dispersive X-ray spectroscopy (EDX), Brunauer-Emmett-Teller (BET) surface area measurement and transmission electronics. TEM, UV-vis diffuse reflectance spectroscopy and acetone degradation tests [4]. Yu S successfully synthesized Bi metal deposited on Bi_2WO_6 composite photocatalyst by simple in-situ reduction method at room temperature using Bi_2WO_6 as self-sacrificing template and $NaBH_4$ as reducing agent. The degree of reduction can be easily adjusted by controlling the concentration of NaBH4 solution. X-ray diffraction (XRD), X-ray photoelectron spectroscopy (XPS), Fourier Transform infrared (FTIR) spectroscopy, N_2 adsorption-desorption isotherms, scanning electron microscopy (SEM), transmission electron microscopy (TEM), high resolution TEM (HRTEM)), diffuse reflectance spectroscopy (DRS) and photoelectrochemical measurements were performed to analyze the phase, morphology, optical properties and photoelectrochemical properties of the samples prepared. Degradation of phenol in visible light (λ> 420nm) was used to investigate the photocatalytic activity, which showed that BWO-0.2 photocatalyst showed the highest efficiency, more than 3 times that of pure Bi_2WO_6 [5]. Zhang J proposed a new layered PD-Bi_2WO_6 structure decorated with different Pd and Bi mole ratios, which has been manufactured by hydrothermal process and chemical deposition methods. He investigated the photocatalytic activity of pure bismuth tungstate and PD-Bi_2WO_6 nanocatalites for the degradation of rhodamine B(RhB) dye and phenol in visible light. His photocatalytic results show that pD-Bi_2WO_6 nanocomposites have significantly enhanced photocatalytic activity. In particular, Bi_2WO_6 loaded with 2.0% Pd showed the highest photocatalytic activity, and almost completely degraded 30mg/L RhB and 10mg/L phenol in 50 and 60 minutes, respectively. In addition, photogenic holes (H +) and O_2 play key roles in the degradation of RhB. According to the experimental results, he also proposed the photocatalytic degradation mechanism of PD-Bi_2WO_6. The enhanced photocatalytic activity is attributed to the combination of efficient separation of electrons and holes, which improves the photocatalytic activity [6]. Ji X has synthesized one-dimensional Ce-doped LiTiO (LiTiCeO, X = 0, 0.01, 0.02, and 0.05) submicrobands of approximately 500 nm in width and approximately 200 nm in thickness using a simple electrostatic spinning method. The structure and morphology of the samples prepared by him were characterized by XRD, TEM, SEM, BET, HRTEM, XPS and AFM. Importantly, he can preserve the one-dimensional $LiTiO_2$sub microstrip well by introducing Ceions, while CeOimpurity can be obtained when x is greater than or equal to 0.02. Ce-doped $LiTiO_2$ electrodes exhibit superior electrochemical properties than their undoped counterparts. In particular, the $LiTiO_2$ electrode has a reversible capacity of up to 139.9mah and remains at 132.6mah after 100 cycles at a 4C current ratio. The excellent lithium storage performance of $LiTiO_2$ electrode can be attributed to its inherent structural advantages and enhanced overall conductivity [7]. Nano-sized catalysts have strong infrared reflection and uv properties, and if added to synthetic coatings, they will form excellent shielding effect in synthetic coatings and achieve the purpose of uv protection. At the same time, the thermal insulation performance of the coating is also improved.

As a special form of freeze-thaw damage, the freeze-thaw damage in the presence of ice salt is mainly the phased peeling of the surface of the architectural coating, and its failure mode and evaluation mode are similar to cracks in the shell. In the past freeze-thaw tests, it was impossible to correctly evaluate the salt freezing damage in the presence of deicing salt. The existing salt freezing test methods will affect the objective study of the results, so further investigation is needed. This

article studies the salt-freezing resistance of bismuth tungstate coatings for architectural use, and explores ways to improve the salt resistance of architectural coatings by reducing free water. To study the influence of aggregates on the salt freeze exposure of architectural coatings, investigate the influence of construction procedures on the surface quality of architectural coatings and the influence of salt freezing resistance of architectural coatings, and propose reliable construction measures to control the surface quality of architectural coatings.

2. Bismuth Tungstate Resistance to Salt Frost Erosion

2.1. Hydrothermal Method

The hydrothermal reaction can be a phase that cannot be prepared by a solid-phase reaction, or it can be carried out under relatively mild conditions. Compared with other liquid phase methods, the hydrothermal method has obvious advantages, such as high purity and uniform particles. The whole process of the hydrothermal reaction is carried out in an airtight reactor, which effectively avoids pollution. Now most of the hydrothermal reaction powder can be directly manufactured. If it is used without post-evaporation treatment, problems such as mixing of impurities, abnormal particle growth, and secondary crystallization will not occur. On the other hand, bismuth tungstate is synthesized by hydrothermal method. This powder overcomes the shortcomings of large particle size and low purity in the high temperature (2899pu) firing of the traditional solid-phase method, and improves the photocatalytic activity [8]. The process of hydrothermal synthesis of bismuth tungstate nanopowders is shown in Figure 1.

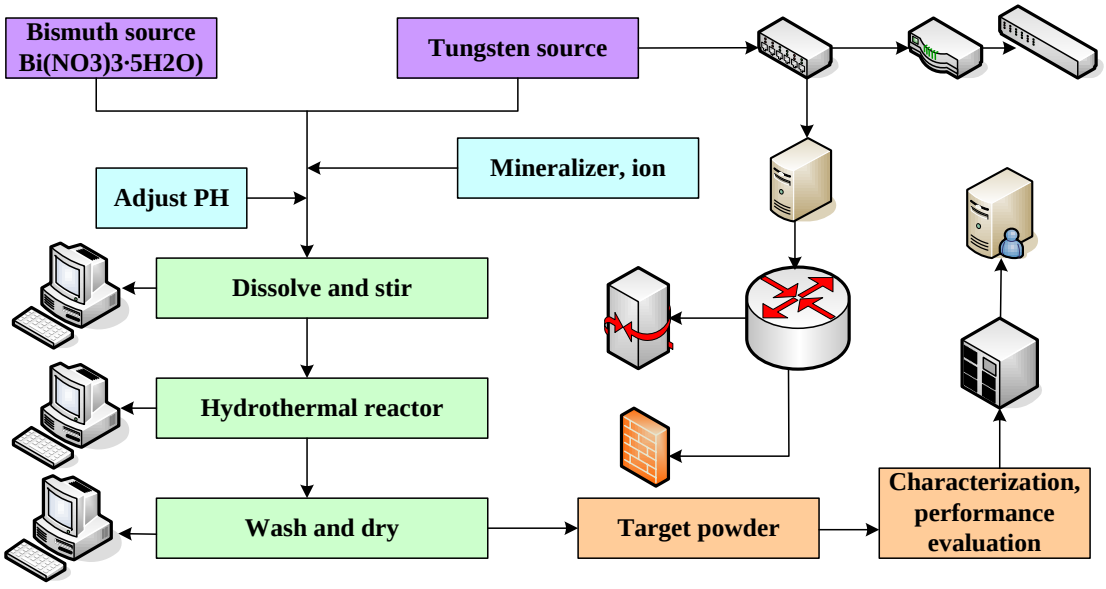

Figure 1. Process for synthesis of Bi2WO6 nano-powder by hydrothermal method

2.2. Preparation of Bismuth Tungstate Photocatalyst

Sodium tungstate solution and bismuth nitrate solution were mixed into 30mL of distilled water (2mL nitric acid (2mol/L) containing 2mmol of bismuth nitrate Bi (NO_3) and 1mol of sodium tungstate (2mol/L) and a certain amount of amino acetic acid). After being put into two 200mL beakers and mixed, the milky white suspension as the precursor of nano-Bi_2WO was obtained. Heat

the beaker containing the Bi_2WO precursor, preheat it to 200℃, and pour it into a constant temperature container with continuous stirring. When the temperature reached the ignition point of $C_2H_5NO_2$, the reaction system began to react automatically as the gas leaked, and light yellow free substances were produced in the beaker. After the self-proliferation reaction is over, the light yellow free substance produced in the beaker is recovered, washed with distilled water and absolute ethanol three times in succession, and dried in a constant temperature oven at 60℃ for 12 hours. The LCM-Bi_2WO powder was prepared. The adsorption and photocatalytic properties of nanomaterials prepared by low-temperature combustion are closely related to the ratio of oxidant to reducing agent. The ratio of bismuth nitrate oxidant and amino acid (C2H5 NO2) is 6:12, 6:10, 6:6, 6:3, 6:2. (Labeled S1, S2, S3, S4, S5), this study investigated their structural properties and photocatalytic performance. The instruments used in the research are shown in Table 1.

Table 1. Instruments used in the research

equipment name	Model	Manufacturer
Xenon lamp	500W	Chengdu Napu Optoelectronics Co., Ltd.
Mercury lamp	500W	Chengdu Napu Optoelectronics Co., Ltd.
Autoclave	HZ5-100L	Shanghai Lei Magnetic Instrument Factory
Electronic balance	ALC-210.4	Beijing Sartorius Instrument System Co., Ltd.
Electric heating constant temperature blast drying oven	GZX-9070MBE	Shanghai Boxun Industrial Co., Ltd. Medical Equipment Factory
Bidirectional magnetic heating stirrer	78-2	Jintan City, Jiangsu Province Ronghua Instrument Manufacturing Co., Ltd.
Ultrasonic cleaner	KQ-250B	Kunshan Ultrasonic Instrument Co., Ltd.
High-speed centrifuge	TGL-10B	Shanghai Anting Scientific Instrument Factory

The light absorption threshold of a semiconductor λ has the following relationship with the band gap E [9]:

$$\lambda = \frac{1240}{E(ev)} \quad (1)$$

The condition for the enhancement of the interference of the reflection lines reflected by the two crystal planes is that the optical path difference between the two is equal to an integer multiple of the wavelength, in the Bragg equation [10-11]:

$$n\beta = 2d\sin\theta \quad (2)$$

Among them, n and d were integers [12].

The semiconductor band gap (Eg) can be calculated by the following formula [13-14]:

$$Eg = 1240/\chi \quad (3)$$

The semiconductor photocatalytic reaction rate follows the Langmiar-Hinshelwood kinetic equation with mathematical form [15]:

$$dC/dT = KC/(1+KC) \quad (4)$$

Among them, C is the molar concentration of pollutants. Combined with the light absorption capacity of the material, the photocatalytic efficiency can be accumulated by the following factors [16]:

$$\varphi = \varphi_{vb} + \varphi_{ab} + \varphi_{cs} + \varphi_{xs} \quad (5)$$

Among them φ_{vb} is the sunlight utilization efficiency, φ_{ab} is the light absorption efficiency, and φ_{cs} is the separation efficiency of electron-hole pairs [17].

$$\Delta F = \frac{F_0 - F_C}{F_C} \times 100\% \quad (6)$$

F_0 is the average value (MPa) of the compressive strength of the comparative test piece.

$$\Delta W = \frac{G - G_N}{G} \quad (7)$$

G is the average mass of the specimen before the freeze-thaw cycle [18].

The relative dynamic elastic modulus M of concrete after N freeze-thaw cycles is calculated with the average value of 3 specimens [19].

$$M = \frac{F_N^2}{F_0^2} \times 100\% \quad (8)$$

2.3. Representation

(1) X-ray diffractometer (XRD)

Use X-ray diffractometer (XRD), BRUKERD-8X Advance X-ray diffractometer to analyze the phase structure of the sample, CuKα radiation (1=0.1542nm), light tube voltage and current 40kV, light tube current 30mA, scanning step length 0.02, The scanning range is 109~70.

(2) Field emission scanning electron microscope (SEM):

In order to observe the morphology of the sample, use a field emission scanning electron microscope (SEM), a JSM-6700F cold field emission scanning electron microscope (JSM-6700F). The acceleration voltage is 30kV.

$$2D\sin\theta = N\varphi \quad (9)$$

$$D=L/(B_M/2\cos\theta) \quad (10)$$

In the formula, D is the average size of crystal grains, and K is a constant [20].

$$K = P \times N/300 \quad (11)$$

K is the durability coefficient, and N is the number of freeze-thaw cycles [21-22].

(3) Ultraviolet-visible absorption spectrum

Uv-vis belongs to electronic spectroscopy, which is mainly used to accurately describe the

spectral characteristics of the photocatalyst under ultraviolet and visible light irradiation, and to determine its spectral absorption range and absorption intensity. In this study, the company's UV-3010uV-visible photometer was used to test the optical properties of BWO-TNWS, mainly to investigate whether the spectral response range of the catalyst is in the visible region. The test conditions are as follows: the scanning range is 200-800nm, the scanning interval is 2 seconds, and the $BaSO_4$ standard white board is used as a reference.

(4) Thermogravimetric analysis (TG~DTA)

Instrument model: SHIMADZU DTG-60H. Air is the carrier gas. The measured sample amount is 10-20 mg. Used to confirm the weight loss and heat absorption and release of the sample during the test.

(5) Photocatalytic activity test

Disperse 0.0500 g of the catalyst in 100 mL of 10.0 mgL RhB aqueous solution in a thermostat at 30 ℃. Use 500WXe lamp as light source (λ>420nm). After reaching the adsorption equilibrium in the dark, the light will turn on due to the photodegradation reaction. The absorbance of RhB at 553nm was measured during the reaction. The concentration is calculated according to the Lambert-Beer law.

2.4. Salt-freeze Test Process of Architectural Coatings

(1) Take the freshly mixed architectural paint and put it into φ110×300mm PVC material cylindrical test mold (with bottom cover) in layers, and place it on the vibrating table to vibrate and compact. After 24 hours, remove the bottom cover of the test mold and put it in a standard curing room for curing, and at the same time, the compression and bending test pieces are formed.

(2) Determination of the amount of erosion at the end of 14, 28, 42 and 56 freeze-thaw cycles, the test piece is taken out, the deicing salt solution is filtered, and the erosion slag of the architectural coating is collected.

(3) Salt freezing cycle system. According to the American ASTM C672 test method, a freeze-thaw cycle system of freezing at -17±2.8℃ for 16~18h in a low temperature test box and thawing at room temperature (23±1.7℃) for 6~8h is adopted to make the salt freeze damage of the test piece and The salt freeze damage under natural conditions is similar.

(4) Place the collected building paint stripping residue in an oven at 80 ℃ and dry it to a constant weight, and weigh the mass after the cooling value is at room temperature.

(5) The degree of internal damage during ultrasonic transmission time is reflected by the relative change of dynamic elastic modulus before and after freezing and thawing. The relative change value of the dynamic elastic modulus is determined by measuring the transmission time of the ultrasonic wave passing through the parallel axis 25mm from the surface of the test piece. Before the sample is pre-saturated and thawing, the ultrasonic transmission time was measured after 14, 28, 42 and 56 freeze-thaw cycles. The measuring instrument used NM-4A-I non-metal ultrasonic detection analyzer. For each sample, the transmission time is measured along two mutually perpendicular transmission axes. The coupling point of the mutually perpendicular transmission axes must be the intersection of the diagonals of the rectangular specimen.

The working system is mainly composed of high-voltage transmission and control system, amplification and attenuation program control system, data acquisition system and special microcomputer system. The high-voltage transmission system controls the high-voltage pulse stimulation generated by the synchronization signal. The transducer converts the electrical signal into an ultrasonic signal and sends it to the test medium. In the test, the ultrasonic spectrum of the

transmitter response is 250kHz. The ultrasonic signal is received by the transducer through the measuring terminal and converted into an electrical signal. The received signal is sent to the data acquisition system after automatic gain adjustment of the program amplification and attenuation system. The data acquisition system quickly sends digital signals to a special microcomputer system. The microcomputer mainly obtains the sound parameters of the measuring object by analyzing the digital received signal including the speech time, main frequency, and amplitude. The smart sensor is shown in Figure 2.

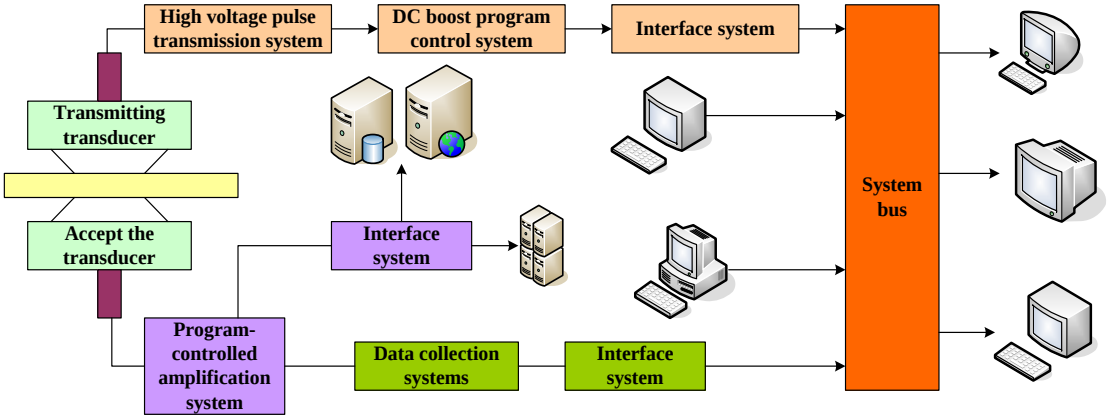

Figure 2. Smart sensor

The corrosion resistance per unit area of the salt-freezing test piece is used to quantitatively evaluate its salt-freezing resistance [23].

$$Q = \frac{m}{A} \quad (12)$$

m is the cumulative amount of erosion (kg) of the specimen after 5n salt freezing cycles. A is the salt-freeze area of the concrete specimen.

3. Research Results of Bismuth Tungstate in Architectural Coatings

In order to study the effect of the amount of bismuth tungstate compound on the crystal structure of the photocatalyst, a series of photocatalyst reactions with different compound ratios were analyzed by XRD. The XRD of the BWO-TNWS composite catalyst samples with different composite ratios is shown in Figure 3. It can be seen from Fig. 3 that the diffraction peaks (133) and (262) of bismuth tungstate with strong crystal planes (131), (060) and (202) are consistent with the orthorhombic bismuth tungstate powder. In addition, there is no diffraction peak, the peak shape is clear, and the crystallinity is pure phase bismuth tungstate. After TNWS and bismuth tungstate nanoparticles are compounded, the characteristic diffraction peaks are obvious, and the crystal structure is not affected. With the increase of the ratio of bismuth tungstate in the composite material, the characteristic diffraction peak of bismuth tungstate has been greatly strengthened, and the characteristic diffraction peak of TNWS has been greatly reduced, indicating that there is a specific difference between TNWS and bismuth tungstate nanoparticles at the interface. Form a heterogeneous structure, resulting in effective recombination.

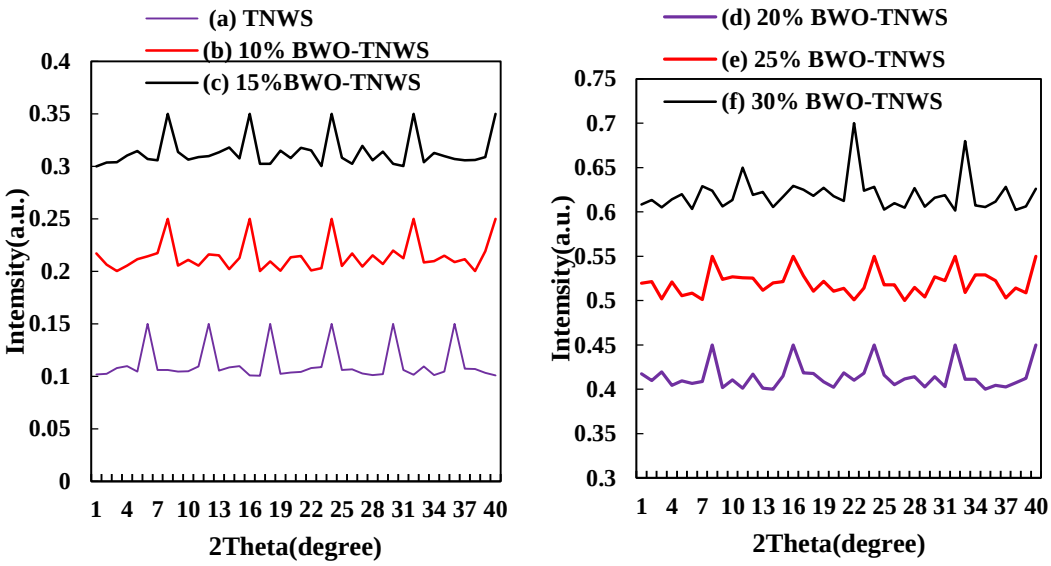

Figure 3. XRD of BWO-TNWS composite catalyst samples with different composite ratios

The 20% BWO-TNWS composite catalyst was selected as the test object, and the ultraviolet-visible absorption spectrum of the degradation liquid in each time period was measured as shown in Figure 4. It can be seen from Figure 4 that as the decomposition time increases, the absorption peak of RhB at 553nm gradually decreases. This indicates that the chromophoric group of the pigment is continuously destroyed. The absorption peak of RhB shows a blue shift associated with the deethylation process of RhB, indicating the gradual decomposition of RhB.

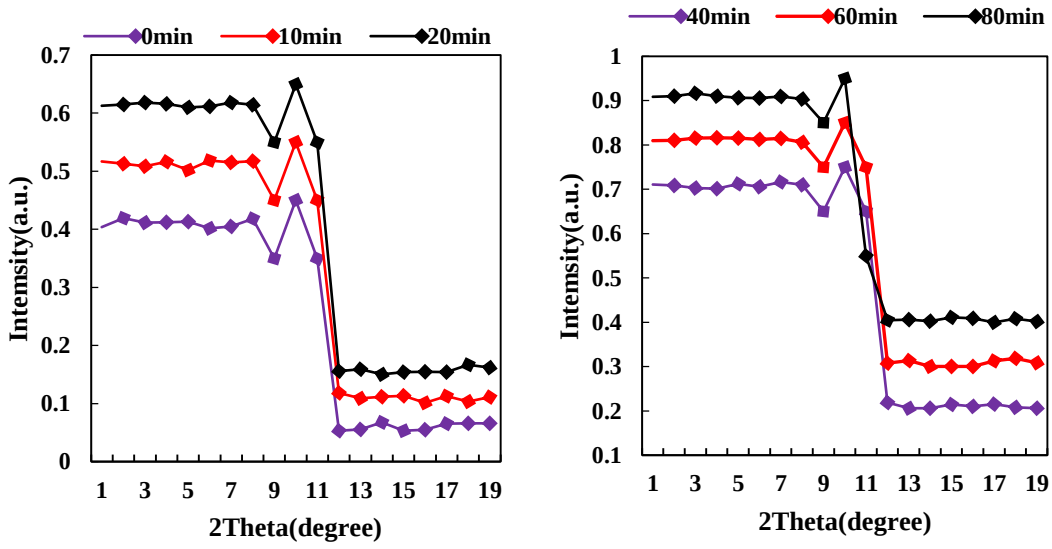

Figure 4. Measure the UV-Vis absorption spectrum of the degradation liquid in each time period

Since the cycle performance of the catalyst is an important index for studying the reutilization capacity of the catalyst, in order to further study the cycle performance of the 20% AgI/Bi_2WO_6 composite catalyst of Rhodamine B, the experimental results of 3 cycles are shown in Figure 5.

Figure 5 shows three periodic decompositions after the decomposition efficiency exceeds 85%, indicating that the stability of the sample is relatively good. It was found that the position and width of the main XRD diffraction peaks of the AgI/Bi_2WO_6 composite catalyst did not change much after 3 cycles. This indicates that the composite photocatalyst still maintains a good crystal structure after several dark state adsorption and photolysis processes. The catalyst has good cycle stability.

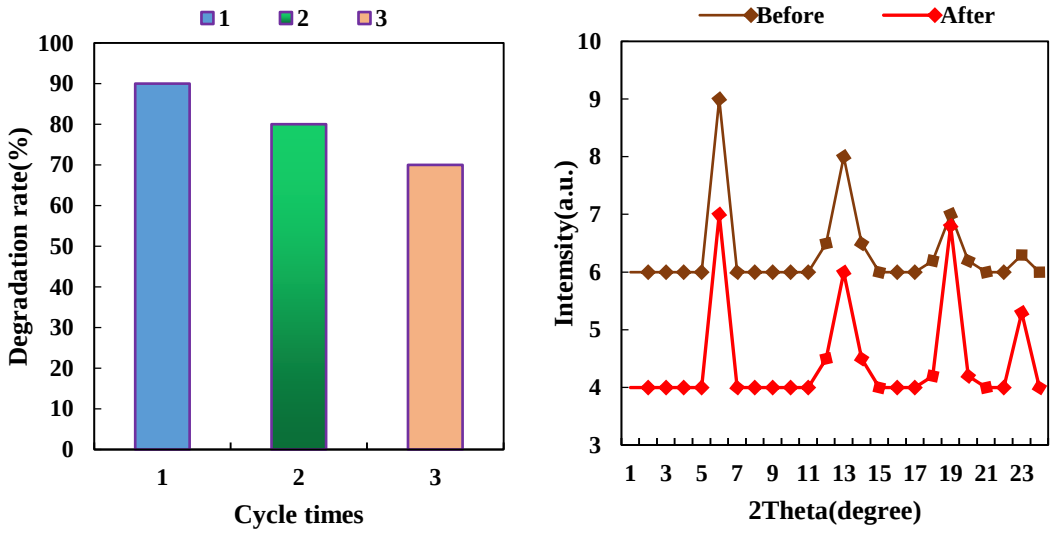

Figure 5. The results of three cycles of the sample

The calculated band gap value of $AgI/Bi_2WO_6/Ag_3VO_4$ composite catalyst is 2.29 eV, and only the band gap value of Ag_3VO_4 is 1.91 eV. The band gap value of the composite three-way catalyst is not as small as when Ag_3VO_4 reacts alone, but it is greatly improved compared to bismuth tungstate (2.71eV) and AgI (2.8eV). In the surface REDOX reaction under visible light, this may be one of the reasons for the improved photocatalytic decomposition efficiency. The estimated result of the band gap value is shown in Figure 6.

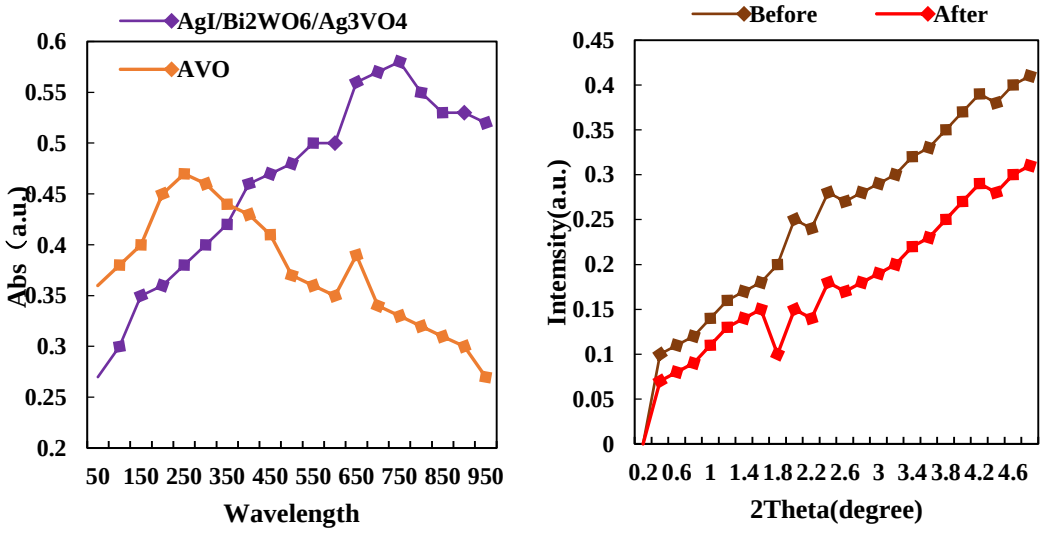

Figure 6. Estimated result of band gap value

With the increase of the number of carbon atoms in the positive ionic alkyl chain of the ionic liquid, the crystallite size of the catalyst prepared by the ionic liquid gradually decreases, which is beneficial to the improvement of the photocatalytic activity. The photocatalytic activity is shown in Table 2.

Table 2. Photocatalytic activity

Catalyst	Grain diameter (nm)
BWO-2-15-20	34.5
BWO-4-15-2	20.3
BWO-4-15-8	21.1
BWO-4-15-16	19.9
BWO-4-15-20	35.1
BWO-4-15-24	38.3
BWO-4-0-20	52.9

The growth of the ionic liquid on the catalyst crystal is shown in Figure 7. Ionic liquids obviously hinder the crystal growth of the catalyst. As the dosage of IL increases, the particle size of the sample decreases. However, if the amount of IL continues to increase, the excess IL will result in a higher density of the catalyst and a decrease in specific surface area. As a result, the activity will decrease. The activity of the crushed BWO-4-15-20-G sample was reduced compared with that before crushing. This is believed to be due to the destruction of the original empty crystal structure after pulverization and the weaker visible light absorption of the catalyst.

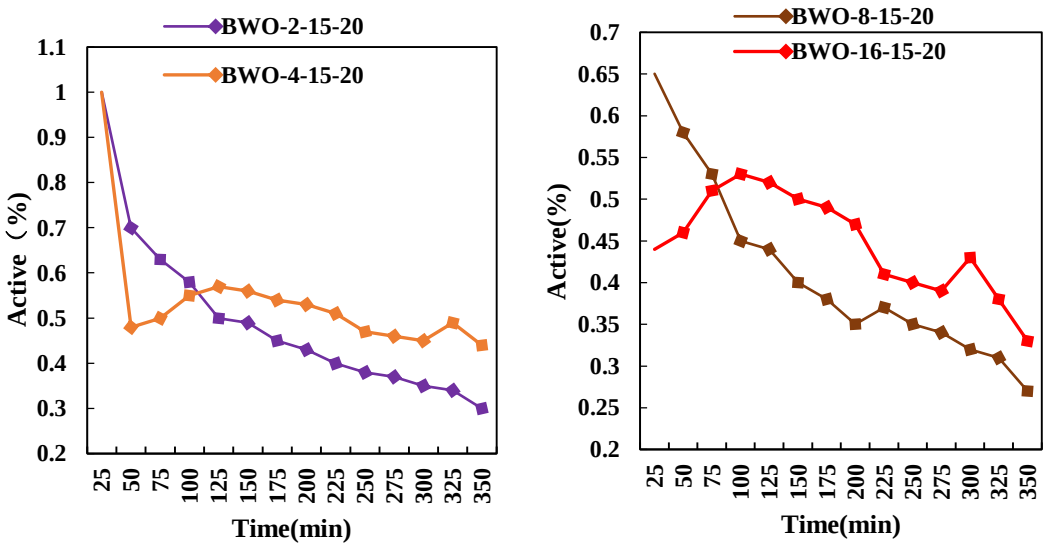

Figure 7. Ionic liquids on the growth of catalyst crystals

The results of inductively coupled plasma spectroscopy (ICP) are shown in Table 3. Silver species are formed on the surface of the catalyst after photoreduction under a UV lamp with a wavelength of 365nm. At the same time, with the extension of the photoreduction time, the actual silver content in the sample tends to increase, which is related to the improvement of the photocatalytic activity. When the fixed photoreduction time is 20 minutes, the actual silver content of the sample gradually increases with the increase of NaG/NW, which helps to improve the photocatalytic activity.

Table 3. Results of inductively coupled plasma spectroscopy (ICP)

Entry	Catalyst	n_{Ag}/nw (%)
1	Ag/BWO-0.50%-20	0.1415
2	Ag/BWO-0.75%-20	0.1759
3	Ag/BWO-1.00%-20	0.1777
4	Ag/BWO-0.75%-15	0.1007
5	Ag/BWO-0.75%-25	0.1731

The XRD patterns of different Ag/BWO samples prepared by the photoreduction method are shown in Figure 8. It can be seen that the prepared samples are all pure orthorhombic bismuth tungstate crystal phases (PDF 39-0256), no other crystal phases are formed, and the crystallinity is relatively high. The diffraction peak of Ag does not appear in the spectrum, which is mainly due to the low and scattered Ag content.

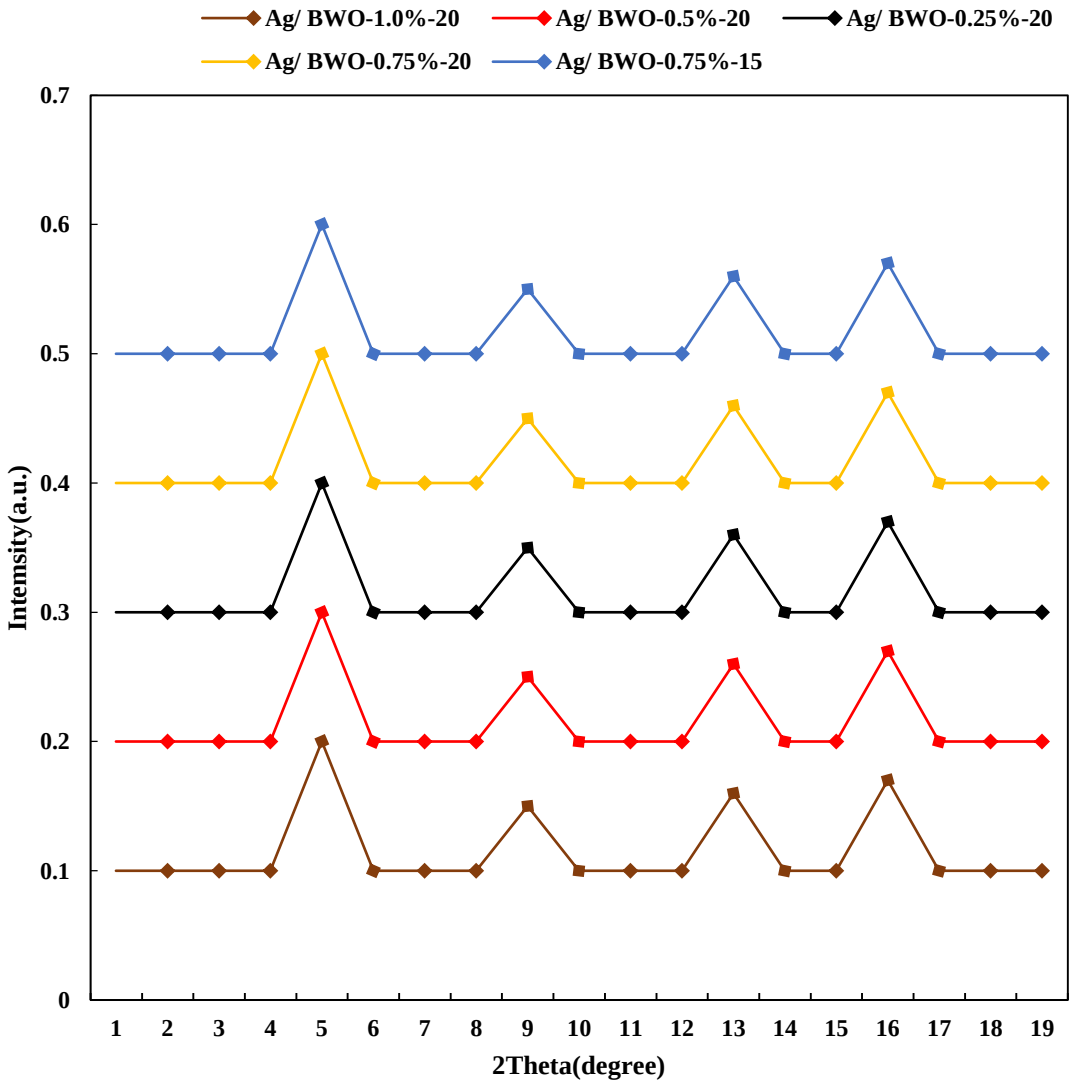

Figure 8. XRD patterns of different Ag/BWO samples prepared by photoreduction method

The analysis results of the range R are shown in Table 4. From the analysis of the range R, it can be seen that the mass ratio of bismuth tungstate and catalyst has the greatest influence on the load rate, followed by temperature and the amount of PVA, and the mass ratio of bismuth tungstate and the volume of the mixed solution has the least influence. The main reason that affects the catalytic loading rate is the mass of bismuth tungstate and the volume ratio of the mixed solution (gL), and the secondary reason is the temperature, the amount of PVA, and the mass of bismuth tungstate and the volume ratio of the mixed solution.

Table 4. Analysis results of very poor R

Experiment number	PVA added amount (mmol)	Sponge to catalyst mass ratio	Temperature(℃)
1	0.02	1: 125	60
2	0.02	1: 0.50	80
3	0.02	1: 075	100
4	0.02	1: 1.00	120
5	0.04	1: 125	100
6	0.04	1: 0.50	120
7	0.04	1: 075	60

The bismuth tungstate is 20%, 40%, and 5% respectively. With low water binder ratio (0.30~0.35), in order to ensure the necessary workability, a highly efficient water reducing agent is used. The compressive strength and flexural strength at each time were measured, the amount of peeling per unit area (mass loss) of the test piece surface after 50 salt-aging cycles was measured, and the damage state of the test piece surface was recorded by photography. According to ASTMC672 classification evaluation, the test coordination ratio is shown in Table 5.

Table 5. Test mix ratio

Serial number	W/CM	Water (kg/m^3)	S slump (mm)	Air content (%)
N9	0.45	I 57	120	>10
N20	0.40	140	40	3.5
N21	0.30	99	190	4.3
N25	0.35	122	110	4.0
M1	.0.33	119	100	5.2
M2	033	119	I 25	4.8

The effect of bismuth tungstate content on architectural coatings is shown in Figure 9. The penetration quality and penetration depth of the deicing salt solution containing 30% bismuth tungstate (FA3+MA) is higher than that of 16.7% bismuth tungstate (FA2+MA). This is because the activity of bismuth tungstate is low in the initial stage.

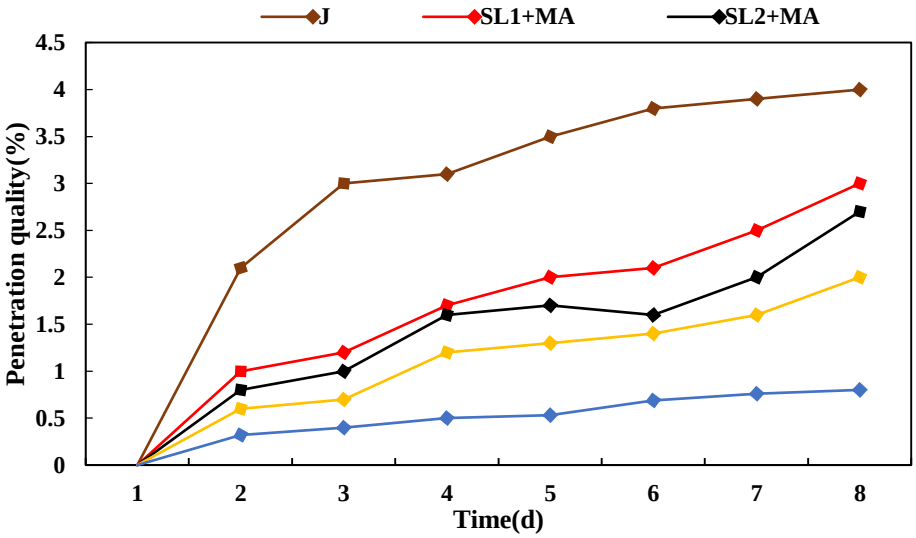

Figure 9. The effect of bismuth tungstate content on architectural coatings

After 10 repetitive loads, the amount of salt-freezing peeling and the relative dynamic elastic modulus loss rate of the architectural coating increased with the increase of the load level. When the load level increased from 0 to 40%, the amount of salt-freezing peeling increased to 1.9 times, and the relative dynamic elastic modulus loss rate increased to 2.3 times. Figure 10 shows the amount of frost erosion after cyclic loading.

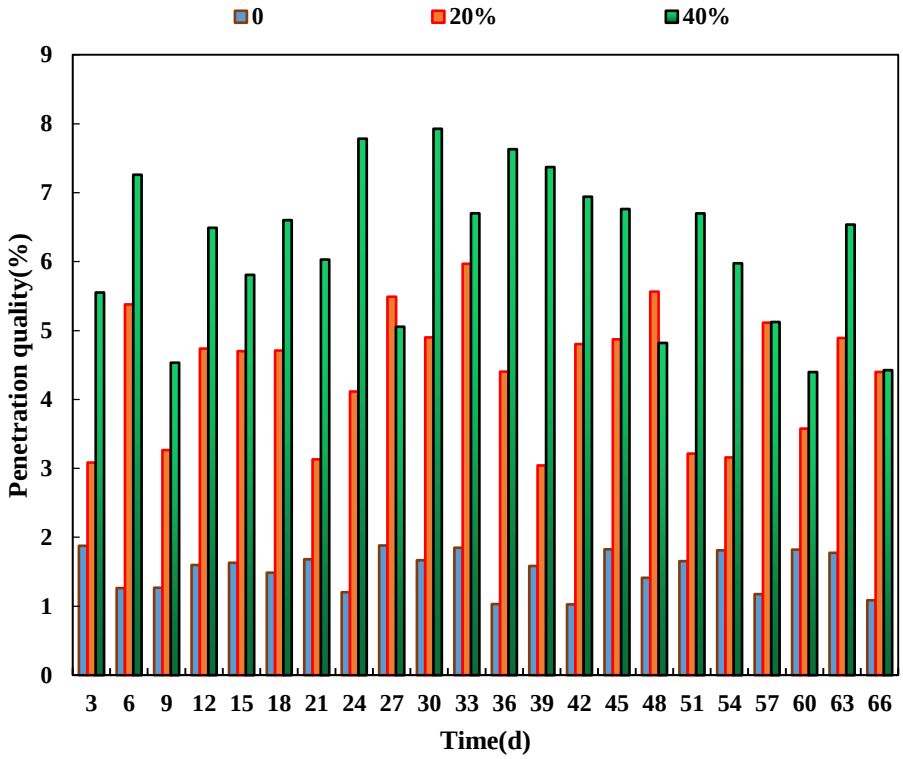

Figure 10. The amount of frost erosion after cyclic loading

4. Discuss

Hydrothermal-solvothermal synthesis means that the reactants are in a high temperature and high pressure state under specific conditions at a specific temperature and pressure, and the reaction is in a critical or subcritical state. In this case, the material has special physical and chemical properties and can simply produce special products. With the development of application technology, hydrothermal method is more and more widely used in crystal preparation. The most commonly used method in the synthesis of bismuth tungstate is the hydrothermal-solvothermal synthesis method [24]. In the architectural coating industry, the pigments and fillers of the coating play an important role, but it is mainly composed of the main film-forming material together with the main film-forming material only through the function of the main film-forming material. Since it is not separated from the membrane itself, it is usually referred to as a secondary film-forming substance. Its main function is to display various colors and covering power on the film, improve the hardness of the coating, delay the damage caused by ultraviolet rays, and improve the durability of the coating.

Depending on the variety of architectural coatings, the quality of the product is also different. Some products can have physical properties in the container during storage. In order to confirm that there is no problem, the paint must be tested in the container before use. In order to confirm quality changes and storage stability, storage tests were implemented under specific conditions. The nano-air purification coating developed in Germany is widely used in bridges, highways, buildings, etc. Japan's nano-photocatalytic coating is in a leading position in the world and has achieved commercial production. Its photocatalytic coating has sterilization, self-purification, deodorization, mold, and can also prevent infections of various diseases. South Korea and Russia have also applied nano-materials in the development of coatings, especially in the anti-bacterial function of nano-coatings, and their products have excellent anti-bacterial properties [25-26].

Bismuth tungstate is one of the newly developed visible light-driven photocatalysts and has received a lot of attention. In recent years, a large number of bismuth tungstate matrix composite materials with micro/nano structure have been prepared, including bismuth tungstate nanosheets, nanoparticles, films, and other element-doped bismuth tungstate matrix composite materials. The change of bismuth tungstate has brought new breakthroughs to the improvement of visible light activity. The composite catalyst based on bismuth tungstate can effectively decompose organic pollutants, disinfect or decompose bacteria. Ionic liquids are usually liquid substances composed of ions at room temperature. Ionic liquids have many characteristics and advantages, and they have attracted more and more attention in the aspects of separation, catalysis, and electrochemistry. As a medium or catalyst for chemical reactions, ionic liquids are widely used in the field of catalysis. Ionic liquids can not only be used as solvents, but can also form H bonds, with various physical and chemical properties. Moreover, its melting point is relatively low, the saturated vapor pressure is very small, it is not easy to volatilize, has a certain degree of conductivity, and can be used as a structural guide for adjusting the shape of the material [27].

With the development of society, it is required to improve the weather resistance of architectural coatings. Currently, resins with good weather resistance include fluororesin and silicone resin. The fluororesin coating has excellent weather resistance, durability, and chemical resistance, but fluororesin is expensive, so it is limited to a wide range of uses. The silicone modified acrylic resin coating has the same performance as the fluororesin coating and is one-third of the cost of the fluororesin coating. Therefore, it has become an important development direction for super weather resistant architectural coatings. At the same time, with the rapid development of nanotechnology,

new methods have been opened up for the study of high-performance and high-quality architectural coatings.

The bismuth tungstate coating is the main architectural coating. The main chain of the bismuth tungstate copolymer is a saturated structure, and the side chain is a polar ester group. Therefore, the bismuth tungstate copolymer coating has excellent outdoor aging resistance, excellent antibacterial properties, and can adhere to various substrates, excellent gloss retention, color durability, and adaptability to humid environments. Moreover, there are many types of bismuth tungstate monomer [28].

5. Conclusion

With the improvement of living standards and health awareness, people pay more and more attention to environmental protection and the safety of living environment, and the environmental protection requirements of interior decoration materials are becoming more and more stringent. At present, indoor decoration materials contain organic volatile substances such as formaldehyde and toluene, which have a bad influence on indoor air pollution and human health. Traditional inner wall coatings cannot meet the requirements of nanomaterials, such as environmental protection and functionality, excellent photocatalytic performance, and salt freezing resistance. In this study, the emulsion of bismuth tungstate was prepared by radical polymerization of the base material of nano environmental protection water-based coating. Next, the influence of reaction conditions on the polymerization reaction was investigated, and the optimal reaction conditions for optimizing polymerization conditions and preparing materials were established. Appropriate base ratio of ingredients and appropriate additives were selected, a reasonable coating combination was designed, and the characteristics of the coating were tested. In order to further study the impact of photocatalytic nanomaterials on biosafety and ensure its biosafety, it is necessary to investigate whether it has adverse effects on biosafety through specific in vivo experiments, including biological blood, organs, and physiology. The antibacterial properties of the material can be further studied in the future.

Funding

This article is not supported by any foundation.

Data Availability

Data sharing is not applicable to this article as no new data were created or analysed in this study.

Conflict of Interest

The author states that this article has no conflict of interest.

References

[1] Kumar S G , Rao K . Comparison of modification strategies towards enhanced charge carrier separation and photocatalytic degradation activity of metal oxide semiconductors (TiO2, WO3 and ZnO). Applied Surface Science, 2017, 391(PT.B):124-148.

[2] Ma J , Li T , Chao X , et al. Hydrothermal Synthesis and Visible Light Photocatalytic Properties of Bi2O2CO3/Bi2WO6 Composite. Catalysis Letters, 2018, 148(2–3):41-50.

[3] Bansal A , Singhal N , Panwar V , et al. Ex situ Cu(0) nanoparticle mediated SET-LRP of methyl methacrylate/styrene-methyl methacrylate in a biphasic toluene–water system. RSC Advances, 2017, 7(18):11191-11197. https://doi.org/10.1039/C7RA00368D

[4] Ratova M , Kelly P J , West G T , et al. Reactive magnetron sputtering deposition of bismuth tungstate onto titania nanoparticles for enhancing visible light photocatalytic activity. Applied Surface Science, 2017, 392(jan.15):590-597. https://doi.org/10.1016/j.apsusc.2016.09.035

[5] Yu S , Zhang Y , Li M , et al. Non-noble metal Bi deposition by utilizing Bi2WO6 as the self-sacrificing template for enhancing visible light photocatalytic activity. Applied Surface Science, 2017, 391(PT.B):491-498. https://doi.org/10.1016/j.apsusc.2016.07.028

[6] Zhang J , Chen T , Lu H , et al. Hierarchical Bi2WO6 architectures decorated with Pd nanoparticles for enhanced visible-light-driven photocatalytic activities. Applied Surface Science, 2017, 404(MAY15):282-290. https://doi.org/10.1016/j.apsusc.2017.01.294

[7] Ji X , Dong L , Lu Q , et al. Electrospinning preparation of one-dimensional Co2+-doped Li4Ti5O12 nanofibers for high-performance lithium ion battery. Ionics, 2017, 24(9):1-8. https://doi.org/10.1007/s11581-018-2453-2

[8] Chen M , Huang Y , Lee S C . Salt-assisted Synthesis of Hollow BiWOMicrospheres with Superior Photocatalytic Activity for NO Removal. Chinese Journal of Catalysis, 2017, 38(2):348-356.

[9] Ji X , Dong L , Lu Q , et al. Electrospinning preparation of one-dimensional Co2+-doped Li4Ti5O12 nanofibers for high-performance lithium ion battery. Ionics, 2017, 24(9):1-8. https://doi.org/10.1007/s11581-018-2453-2

[10] Jiang L , Wang S , Shi L , et al. Solvothermal Synthesis of TiO2/Bi2WO6 Heterojunction Photocatalyst with Optimized Interface Structure and Enabled Photocatalytic Performance. Chinese Journal of Chemistry, 2017, 35(002):183-188. https://doi.org/10.1002/cjoc.201600563

[11] Dai W , Yu J , Deng Y , et al. Facile synthesis of MoS2/Bi2WO6 nanocomposites for enhanced CO2 photoreduction activity under visible light irradiation. Applied Surface Science, 2017, 403(may1):230-239. https://doi.org/10.1016/j.apsusc.2017.01.171

[12] Wang M , Jin Z , Liu M , et al. Nanoplate-assembled hierarchical cake-like ZnO microstructures: solvothermal synthesis, characterization and photocatalytic properties. RSC Advances, 2017, 7(52):32528-32535. https://doi.org/10.1039/C7RA03849F

[13] Wang Z , Hu T , Dai K , et al. Construction of Z-scheme Ag 3 PO 4 /Bi 2 WO 6 composite with excellent visible-light photodegradation activity for removal of organic contaminants. Chinese Journal of Catalysis, 2017, 38(12):2021-2029.

[14] Zheng C , Hua Y . Assembly of Ag3PO4 nanoparticles on rose flower-like Bi2WO6 hierarchical architectures for achieving high photocatalytic performance. Journal of Materials Science: Materials in Electronics, 2018, 29(11):9291-9300.

[15] XianghuiZhang, WeizhuoGai. Effect of surfactant on the photocatalytic activity of Bi2WO6 nanoparticles. Journal of Materials Science: Materials in Electronics, 2017, 28(13):9777–9781.

[16] Xin Y K , Tan W L , Ng B J , et al. Harnessing Vis–NIR broad spectrum for photocatalytic CO2 reduction over carbon quantum dots-decorated ultrathin Bi2WO6 nanosheets. Nano Research, 2017, 10(005):1720-1731. https://doi.org/10.1007/s12274-017-1435-4

[17] Xing, Pengfei, Zhao, et al. Preparation of Bi_2WO_6 and Its Ultra-Deep Oxidative Desulfurization Performance in Ionic Liquids. China Petroleum Processing & Petrochemical

Technology, 2017, 01(v.19):102-108.

[18] Feng Y , Lai S , Yang L , et al. Polymer-derived porous Bi2WO6/SiC(O) ceramic nanocomposites with high photodegradation efficiency towards Rhodamine B. Ceramics International, 2018, 44(7):8562-8569.

[19] D Hao, Yin Y , Guo X . Synthesis and characterization of Ag/Bi2WO6/GO composite for the fast degradation of tylosin under visible light. Environmental Science and Pollution Research, 2018, 25(1):1-13. https://doi.org/10.1007/s11356-018-1296-8

[20] Zhang X , Yu S , Liu Y , et al. Photoreduction of non-noble metal Bi on the surface of Bi2WO6 for enhanced visible light photocatalysis. Applied Surface Science, 2017, 396(PT.1):652-658.

[21] Zhao Y , Wang Y , Liu E , et al. Bi 2 WO 6 nanoflowers: An efficient visible light photocatalytic activity for Ceftriaxone sodium degradation. Applied Surface Science, 2017, 436(APR.1):854-864.

[22] Jonjana S , Phuruangrat A , Thongtem S , et al. Synthesis, characterization and photocatalysis of heterostructure AgBr/Bi 2 WO 6 nanocomposites. Materials Letters, 2018, 216(APR.1):92-96. https://doi.org/10.1016/j.matlet.2018.01.005

[23] Ji X , Dong L , Lu Q , et al. Electrospinning preparation of one-dimensional Ce3+-doped Li4Ti5O12 sub-microbelts for high-performance lithium-ion batteries. Ionics, 2017, 19(12):1-8. https://doi.org/10.1007/s11051-017-4085-2

[24] Zheng X J , Li C L , Zhao M , et al. Photocatalytic degradation of butyric acid over Cu 2 O/Bi 2 WO 6 composites for simultaneous production of alkanes and hydrogen gas under UV irradiation. International Journal of Hydrogen Energy, 2017, 42(12):7917-7929.

[25] Jakhade A P , Biware M V , Chikate R C . Correction to "Two-Dimensional Bi2WO6 Nanosheets as a Robust Catalyst toward Photocyclization". Acs Omega, 2017, 2(10):7219-7229. https://doi.org/10.1021/acsomega.7b01086

[26] Bi H , Liu J , Wu Z , et al. Construction of Bi2WO6/ZnIn2S4 with Z-scheme structure for efficient photocatalytic performance. Chemical Physics Letters, 2021, 769(3-4):138449. https://doi.org/10.1016/j.cplett.2021.138449

[27] Phu N D , Hoang L H , Guo P C , et al. Study of photocatalytic activities of Bi2WO6/BiVO4 nanocomposites. Journal of Sol-Gel Science and Technology, 2017, 83(3):640-646. https://doi.org/10.1007/s10971-017-4450-8

[28] Zhang L , Yang C , Lv K , et al. SPR effect of bismuth enhanced visible photoreactivity of Bi2WO6 for NO abatement. Chinese Journal of Catalysis, 2019, 40(5):755-764. https://doi.org/10.1016/S1872-2067(19)63320-6